Highly Ordered Nanoporous β-Ni(OH)₂ Nanobelt Array Architectures as Electrode Material for Electrochemical Capacitors: Design, Synthesis, Characterization and Supercapacitive Evaluation

Zahra Norouzi ǀ Seyed Heydar Mahmoudi Najafi* ǀ Sayed Ahmad Mozaffari*

*Department of Chemical Technologies, Iranian Research Organization for Science and Technology (IROST), Tehran, 33535111, Iran
E-mail: mahmoudi@irost.ir , mozaffari@irost.ir

Abstract

The electrochemical performances derived from the supercapacitors extremely depend on their morphology. Indeed, designing nanostructured electrode materials has a dramatic role in supercapacitor technology. Herein, highly ordered nanoporous Ni(OH)₂ nanobelt arrays were synthesized using a mild wet-chemical route. Ammonia and persulfate concentrations were found to be important factors controlling the formation of the nanobelt array architecture. The as-prepared nanobelt arrays were characterized using FE-SEM, FT-IR, XRD, and EDX analysis. The obtained Ni(OH)₂ nanobelt electrode exhibited a specific capacitance of 384 mF cm² at 1.0 mA cm², fast rate performance, and excellent cycle life. These notable electrochemical features were attributed to the morphology of highly ordered nano-array architectures, which provides numerous free channels and offers more electroactive sites and sufficient buffering space to moderate inner mechanical stress and minimize the ion transfer path during the redox reactions. These nanoporous Ni(OH)₂ nanobelt arrays were suitable candidates as advanced electrode material for supercapacitor applications.

Abbreviations

Charge transfer resistance (R_{ct}), Continuous cyclic voltammetry (CCV), Cyclic voltammetry (CV), Electrical doublelayer capacitors (EDLCs), Electrochemical capacitance (Q_c), Electrochemical impedance spectroscopy (EIS), Electrolyte resistance (R_s), Energy dispersive X-ray spectroscopy (EDX), Equivalent series resistance (ESR), Field-emission scanning electron microscope (FE-SEM), Fourier transform infrared spectroscopy (FTIR), Galvanostatic chargedischarge (GCD), Highly ordered nanoporous $Ni(OH)_2$ nanobelt arrays (HONNA), Ion diffusion resistance (Z_w), Layered double hydroxide (LDH), Nickel hydroxide (($Ni(OH)_2$), Nickel oxide (NiO), N-Methyl-2-pyrrolidone (NMP), One-dimensional (1D), Polyvinylidene fluoride (PVDF), Potassium persulfate ($K_2S_2O_8$), Stainless steel (SS), Supercapacitors (SCs), Transition metal oxides (TMOs), Two-dimensional (2D), X-ray diffraction (XRD).

1. Introduction

Recently, due to the increase in greenhouse gasses, the fast diminution of fossil fuel sources, environmental pollution, and global warming issues have drawn considerable attention. Therefore, there is a serious demand to design clean, safe and renewable energy storage systems.

Supercapacitors (SCs) are considered as main energy storage systems. They have a large output potential, low self-discharge, high power density, long cycle life, safety operation, and no memory effect. They are extensively used in portable electronic devices e.g., cellphones, laptops, digital cameras, and electric vehicles, etc. [1], [2].

The electrical doublelayer capacitors (EDLCs) are the most common version of supercapacitors which use carbon-based materials. However, the energy density derived from these kinds of supercapacitors is low and does not fulfill the highenergy and powerdensity requirements of electronic vehicles [3].

The pseudocapacitive version of supercapacitors, which store charges based on reversible faradaic reactions at the interface of electrode/electrolyte, demonstrates higher electrochemical performances compared with EDLC ones [4]. Fast redox reactions result in high electron transport in the electrode to the current collector and fast ion transfer in the electrolyte surrounding the electrodes. Hence, to meet practical requirements, pseudocapacitive electrode materials should be employed parallel to EDLCs.

One-dimensional (1D) nanostructures (e.g., nanorods, nanowires, and nanotubes) or two-dimensional (2D) nanostructured materials (nanobelts and nanosheets) fulfill such requirements due to their high surface area and ideal charge transfer channels caused by void spaces between neighboring groups [4], [5]. It is expected that oriented 1D and 2D nanostructure arrays facilitate the charge-discharge kinetics in supercapacitors and exhibit better electron transfer ability than 0D nanomaterials [6], [7]. Thus, the 2D architectures will be desirable in achieving highrate pseudocapacitive performances.

Besides the role of morphology, electrode material selection is critical in the supercapacitor performance as well. Recently, transition metal oxides (TMOs) have been widely used as supercapacitor electrode material owing to high specific capacitances [8], [9]. Among them, nickel oxide (NiO) and nickel hydroxide ($Ni(OH)_2$) are of crucial importance owing to their high specific capacitances, environmental friendliness, high thermal and chemical stability, and lowcost issues [10].

Although traditional powder TMOs have high theoretical capacitance, their electrochemical performance does not fulfill the operative demands. Most TMOs are semiconductors or even insulators, and display minor electrical conductivity and involve high volume expansion, leading to deterioration during the ion intercalation/de-intercalation and resulting in poor

cycle life and supercapacitive performance [11]. Due to these disadvantages, the improvement of TMOs for use in supercapacitors is significantly limited. So designing ordered nanostructure array electrode materials such as nanowalls [12], nanosheets [13], nanobelts [14], nanotubes [15], and nanowires [16] is a great solution to avoid the abovementioned issues [17].

Several $Ni(OH)_2$ nanostructures have been synthesized using template-assisted, electrodeposition, hydrothermal, and anodic deposition methods [7]. Nevertheless, these nanotubes/nanowires are randomly aligned rather than oriented [6]. The vertically oriented 1D or 2D $Ni(OH)_2$ nanostructures have been rarely investigated [6].

In this study, highly ordered nanoporous $Ni(OH)_2$ nanobelt arrays (HONNA) were synthesized using simple one step hydrothermal method as an efficient electrode material for supercapacitive applications. We focused on enhancing the electrochemical performance of SCs by developing HONNA through a controlled, low temperature and mild wet-chemical route. This method has the advantage of controlling the crystal growth and morphology of the material. Benefiting from its single crystalline nature and vertically alignment, the -$Ni(OH)_2$ (111) nanobelt arrays can be used as a promising electrode material for supercapacitors. The nanobelt array architecture prevents accumulation or leakage of the electrode materials. Furthermore, it provides a large number of accessible voids, accelerating the charge transfer and shortening the ion diffusion path. So, it is probable that HONNA be a favorable candidate for the next generation of supercapacitors.

2. Experimental section

2.1. Synthesis of highly ordered nanoporous $Ni(OH)_2$ nanobelt arrays

All reactants were of analytical grade and used as received. Before starting the experiment, stainless steel (SS) substrates were cleaned by ultrasonication in 3 M HCl, alcohol, acetone, and distilled water for 10 min.

The HONNA were synthesized via a wet-chemical route. In a typical procedure, 45 mL of distilled water was used to dissolve 5.26 g $Ni(SO_4)_2.6H_2O$ and 1.0 g potassium persulfate ($K_2S_2O_8$). Then, 5 mL of condensed (25–28%) aqueous ammonia was added dropwise. The reaction was performed in a Teflon-lined stainless-steel autoclave at 150 °C for 8 h followed by cooling down the autoclave to ambient temperature. This protocol resulted in the formation of green HONNA sample. The product was centrifuged and then cleaned with deionized water and alcohol repeatedly to remove any impurities followed by drying at 80 °C in an electric oven.

2.2. Structural characterization

A field-emission scanning electron microscope (FE-SEM; TESCAN Mira II, Japan) equipped with energy dispersive X-ray spectroscopy (EDX) was used to monitor the morphological topographies and elemental composition of the product. Fourier transform infrared spectroscopy (FT-IR, Bruker, TENSOR 27, USA) was applied to identify the functional groups of the product in the range of 4000–400 cm^{-1} under transmittance mode. The crystalline nature of the product was studied using X-ray diffraction (X-Ray Diffractometer, Philips PW1730, Netherlands). The as-prepared sample was exposed to Cu-Kα radiation to acquire the diffraction pattern.

2.3. Electrode fabrication and measurements

The working electrode was prepared by blending HONNA (80% w/w), carbon black (10% w/w) as a conductive additive, and polyvinylidene fluoride (PVDF) (10% w/w) as a binder in N-Methyl-2-

pyrrolidone (NMP) solution, and then drop casted into a SS substrate.

The electrochemical measurements were conducted in the half-cell configuration, while the $Ni(OH)_2$ served as working electrode. A Pt plate and an Hg/Hg_2Cl_2 were served as counter and reference electrodes, respectively. An aqueous solution of 3 M KOH was used as the electrolyte.

Cyclic voltammetry (CV) and galvanostatic chargedischarge (GCD) tests were performed with a potentiostat/galvanostat Autolab 302N, the Netherlands, at a potential between 0.0 and 0.5 V. To perform the electrochemical impedance spectroscopy (EIS) analysis, an AC voltage with an amplitude of 5 mV was applied at frequencies between 100 kHz to10 mHz.

3. Results and Discussion

3.1. Morphological evolution of HONNA

The formation process of HONNA is schematically illustrated in **Fig. 1**. HONNA were synthesized by a wet-chemical route at 150 °C for 8 h. To investigate the growth kinetics of HONNA, the effects of growth parameters like precursor, time, and temperature on the morphology evolution of the nanobelt arrays were explored. The growth time played a crucial role in the formation process of HONNA. At reaction times be-

low 6 hours, only a single piece of film was formed. However, by increasing the growth time, the preliminary structure gradually grew and nanobelt arrays began to form. The nanobelt arrays also became thicker and longer with increasing reaction time. When the reaction time was increased to 24 hours, petal-like arrays were produced, which had well-defined crystal structure and high surface area. This suggested that the growth time could be used as a tuning parameter for controlling the crystal growth and morphology of the nanobelt arrays [18]. The obtained nanobelt arrays had an average height about 18 mm.

The temperature also played a key role in the formation of HONNA. At temperatures less than 110 °C, no deposition of nanobelts occurs since crystal growth has not been completed. By increasing the temperature up to 140 °C, severe accumulation of the $Ni(OH)_2$ crystals occurs, signifying the crystal growth above this temperature. By increasing the temperature to 150 °C, $Ni(OH)_2$ crystals were able to achieve enough energy to grow quickly and form nanobelt arrays [6].

The thickness of HONNA could be manipulated by tailoring the growth time, temperature, and precursor concentration. However, it was observed that the growth parameters such as temperature, growth time, Ni^{2+} source and concentration, had minor effects on the final morphology of the
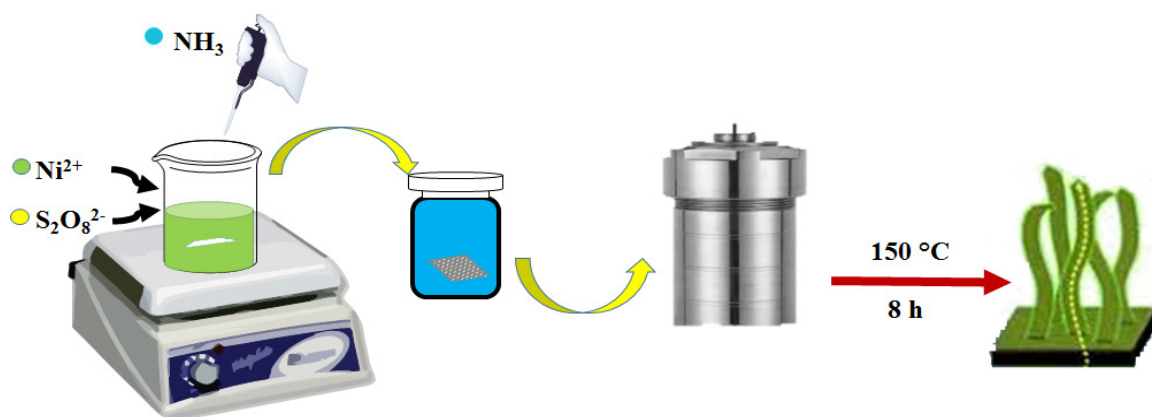

Fig. 1. Schematic illustration of the formation process for the highly ordered nanoporous $Ni(OH)_2$ nanobelt arrays (HONNA).

nanobelt arrays [19]. Increasing these parameters only resulted in thicker films, however, the nanobelt arrays were always formed. This suggested that the formation of nanobelt arrays was primarily governed by the intrinsic properties of the precursor and the growth mechanism. Similar results are expected during the synthesis of $Ni(OH)_2$ nanobelts.

In contrast to other growth parameters, ammonia and persulfate concentration played a crucial role in determining the final architecture of $Ni(OH)_2$ nanobelt arrays. Lower NH_3 concentrations caused $Ni(OH)_2$ to grow quickly even at room temperature, leading to an uncontrolled morphology. For the formation of $Ni(OH)_2$ crystals, greater temperatures were required as NH_3 concentration increased. At higher concentrations of ammonia, shorter but thicker nanobelts were obtained. A high molar ratio of NH_3 to Ni^{2+} resulted in suitable surface adhesion, facilitating the coherence of the surface and leading to a more compact texture. These results suggested that precise control over the concentration of NH_3 was necessary for obtaining well-defined and uniform $Ni(OH)_2$ nanobelt arrays [20]. For better control of the growth of nanobelt arrays, an accurate concentration of ammonia is necessary. Higher ammonia concentrations could prevent the deposition of $Ni(OH)_2$ crystals because of the strong chelate formation of NH_3 with Ni^{2+} cations. This can be explained by the following equation:

$$(1)$$

$$[Ni(H_2O)_{6-x}(NH_3)x]^{2+} + 2OH^- \longleftrightarrow Ni(OH)_2 + (6-x)H_2O + xNH_3$$
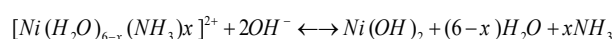
The molar ratio of potassium persulfate was also a critical factor in the growth of HONNA. In the absence of $K_2S_2O_8$, the nuclei had no sufficient energy to grow in a well-ordered manner. As a result, $Ni(OH)_2$ crystals formed in all directions, ultimately resulting in a solid $Ni(OH)_2$ powder instead of highly ordered nanoporous nanobelt arrays.

The nanobelt arrays are developed by the modest layering of hexagonal-shaped nanoplates in the presence of $S_2O_8^{2-}$. By adding persulfate to the reaction medium, the $Ni(OH)_2$ nanosheets gradually grew and changed to a dense nanobelt array structure. This was due to the oxidation of $Ni(OH)_2$ by persulfate, leading to the formation of NiOOH on the surface of the nanoplates. The newly formed NiOOH species then acted as a growth site for the successive deposition of $Ni(OH)_2$. The gradual growth of $Ni(OH)_2$ on the surface of the nanoplates resulted in highly ordered nanoporous nanobelt arrays.

Ions and molecules exist between the stacking layers of $Ni(OH)_2$ due to layered double hydroxide (LDH) nature of $Ni(OH)_2$ [21]nanowires, short nanowires, and β-Ni(OH. In hexagonal $Ni(OH)_2$, the (001) plane is the tightest packed plane. The $S_2O_8^{2-}$ anion is adsorbed on the highly active (001) plane in the presence of $K_2S_2O_8$, deactivating this plane. The selective adsorption of $S_2O_8^{2-}$ onto the exposed (001) plane caused stacking of $Ni(OH)_2$ crystals along the c-axis, resulting in vertically oriented HONNA with numerous electroactive sites. This stacking phenomenon led to increased accessibility of electrolyte ions to more electroactive sites, improving the electrochemical performance of the nanobelt arrays [22].

3.2. Material characterization

The FE-SEM imaging was conducted to inspect the morphological properties and the texture of the obtained β-$Ni(OH)_2$ products. **Fig. 2** reveals the FE-SEM images of the $Ni(OH)_2$ sample in the absence of persulfate. As seen, in this case, only puffy $Ni(OH)_2$ nanoflakes were achieved.

Fig. 3A displays the FE-SEM images of the $Ni(OH)_2$ nanobelt arrays structure at different magnifications. The inset in **Fig. 3A** (scale 2 μm) reveals that the freshly obtained product was green and uniform. Moreover, the welldefined and interconnected nanobelt structure stuck to the SS substrate. The nanobelt motif with a
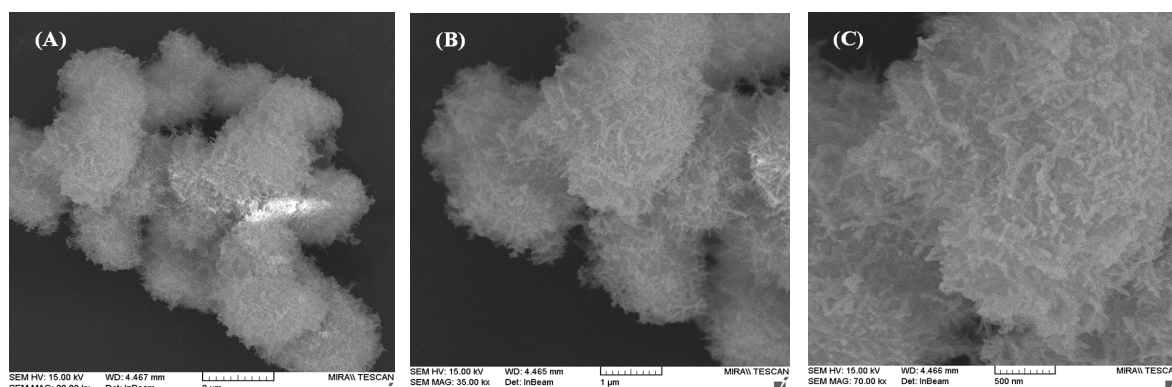
Fig. 2 FE-SEM images of Ni(OH)$_2$ samples in the absence of K$_2$S$_2$O$_8$.

porous texture could be clearly imaged. **Fig. 3B** (scale 1 μm) shows the involved and interconnected Ni(OH)$_2$ nanobelt wound with each other and form the wrinkled HONNA structure. The high magnification (scale 500 nm) of FE-SEM image (**Fig. 3C**) discloses that the nanobelts comprised multilayers of interconnected uniform belts stacked with ultrasmall nanosheets, which were related to the LDH nature of Ni(OH)$_2$ [23]. The Ni(OH)$_2$ nanobelt arrays had an average height around 1-2 μm, a thickness less than 100 nm, and an average pore size almost 7.23 nm. The film thickness can be efficiently manipulated by tuning the growth time without the change in the morphology. According to the FE-SEM results, the Ni(OH)$_2$ array struc-

ture was composed of many interweaving nanosheets. This open structure generated expanded surface area for adequate electrode/electrolyte contact, which reduced the internal stress and sustained the structural strength.

The EDX spectra (**Fig. 4A**) revealed the existence of nickel and oxygen atoms, which are the constituent elements of Ni(OH)$_2$. The corresponding elemental mapping analysis (**Figs. 4B** and **4C**) displayed diffraction spots that were uniformly dispersed throughout the nanobelt array structure, indicating homogeneous distribution of nickel and oxygen atoms. These results confirmed the successful synthesis of HONNA.
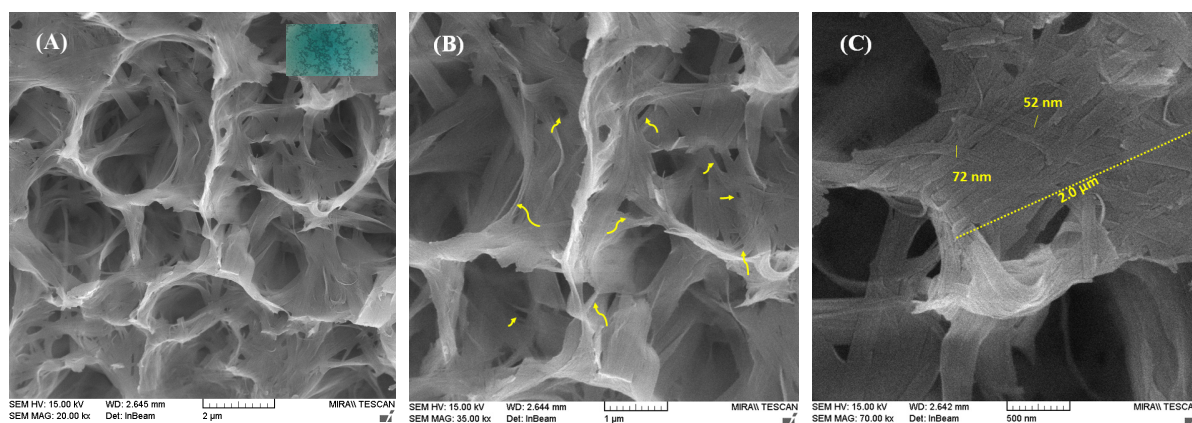

Fig. 3 FE-SEM images of highly ordered nanoporous Ni(OH)$_2$ nanobelt arrays (HONNA) at different magnifications.
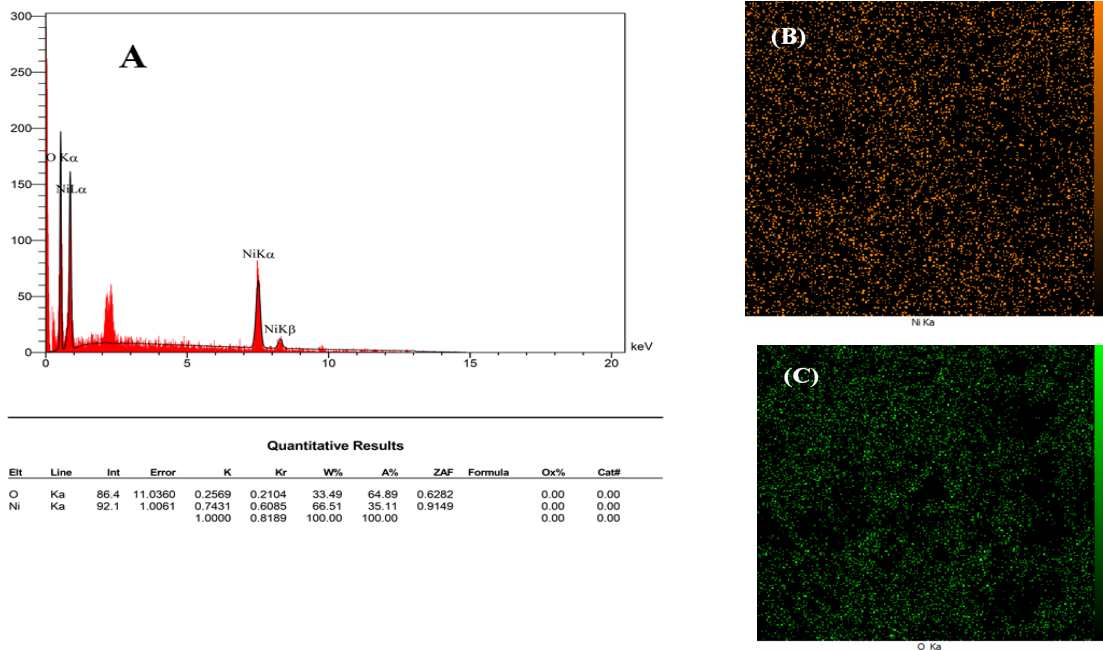
Fig. 4 (A) EDX analysis and (B,C) Elemental mapping of the obtained highly ordered nanoporous Ni(OH)$_2$ nanobelt arrays (HONNA).

The XRD pattern of the HONNA is demonstrated in **Fig. 5**. The pattern shows diffraction peaks at 20.2°, 32.7°, 39.1°, 43.3, 53.2°, and 78.2°, which indexed to the (001), (100), (101), (102), (110) and (111) lattice planes, respectively. This pattern agreed well with standard crystallographic data and could be referred to the hexagonal β-Ni(OH)$_2$ structure (JCPDS card No. 14-0117). The strong and narrow peaks manifested the excellent crystallinity of the highly ordered

nanoporous Ni(OH)$_2$ nanobelt arrays. The high intensity of the (102) diffraction indicates that the as-prepared sample was highly oriented. In addition, no detectable secondary phase was observed. It is notable that the nickel sulfate precursor was entirely transformed to β-Ni(OH)$_2$ since no other miscellaneous peaks were detected in the XRD spectra. This result confirmed that the synthesized nanobelt arrays had a well-defined crystal structure and were of high purity.
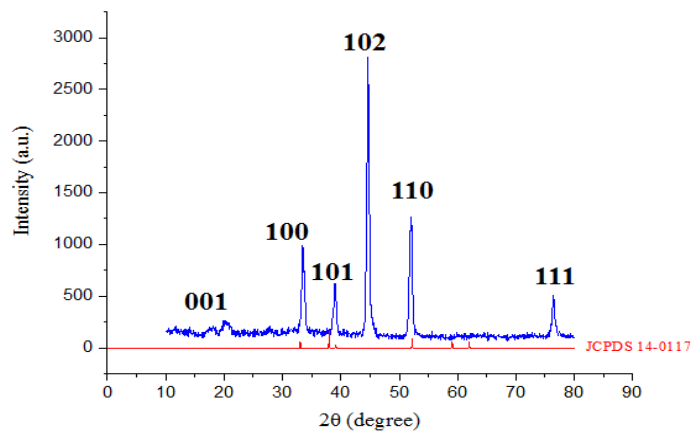

Fig. 5 XRD pattern of the synthesized highly ordered nanoporous Ni(OH)$_2$ nanobelt arrays (HONNA).
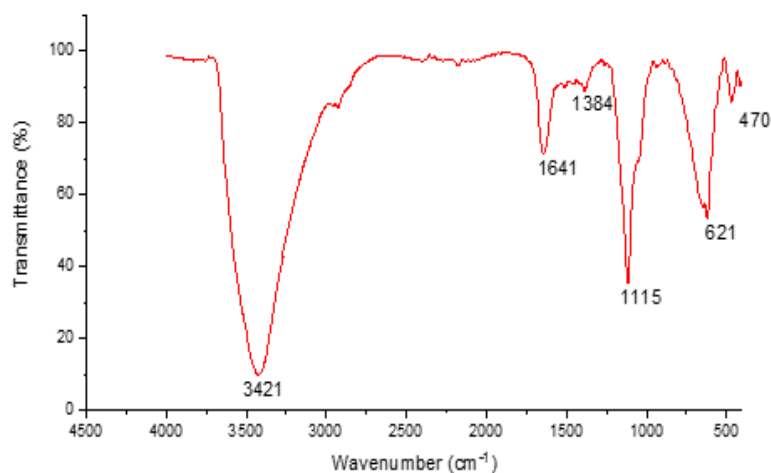
Fig. 6. FT-IR spectrum of the synthesized highly ordered nanoporous Ni(OH)₂ nanobelt arrays (HONNA).

Fig. 6 exhibits the FT-IR spectrum of β-Ni(OH)₂ nanobelt arrays. The main functional groups in βNi(OH)₂ nanobelt arrays were detected by FTIR spectroscopy. The broad absorption band about 3423 cm[1] could be ascribed to O–H stretching vibrations of the physiosorbed water molecules and the hydrogen-bound hydroxyl groups in β-Ni(OH)₂ phase, which approves the brucite nature of nickel hydroxide structure [24], [25]. The peak at 1641 cm^{-1} was associated to the bending vibration of the interlayer water molecules. The strong peak at 1115 cm^{−1} and the small peak at 1384 cm^{−1} relate to the δ O–H and Ni–O stretching modes, respectively [25], [26]. The bands at 621 cm^{-1} and about 470 cm[1] were related to the NiOH bending and Ni-O stretching vibrations, respectively [27].

3.3. Electrochemical evaluation of HONNA for SCs

The deposited HONNA on SS current collector were utilized as the supercapacitor electrode and showed notable electrochemical performance. To study the electrochemical features of the HONNA, a set of electrochemical tests was conducted using CV and GCD measurements and the results are presented in **Fig. 7**. The CV curve of the Ni(OH)₂ nanobelt arrays at a scan rate of 10 mV s[1] is demonstrated in **Fig. 7A**. A

couple of welldefined redox peaks at 0.24 V and 0.34 V were detected, corresponding to Faradaic reactions occurring on the Ni(OH)₂ surface rather than from the adsorption of ions on a double-layer capacitor [28]. These peaks signified the pseudocapacitive nature of the nanobelt arrays, which could be explained by the following equation [4]:

$$Ni\,(OH)_2 + OH^- \leftrightarrow NiOOH + H_2O + e^- \tag{2}$$

Furthermore, the low surface area of the stainless steel substrate used in the synthesis of the Ni(OH)₂ nanobelt arrays indicated that the capacitance arising from the current collector was negligible and did not contribute to electrochemical reactions.

Typically, the kinetics of Faradaic reactions at an electrode surface is ruled by the electron migration process, ion adsorption on the electrode surface, and ion penetration in the electrolyte solution surrounding the electrodes [29]. For determining the rate-limiting process, CV tests were conducted at different scan rates ranging from 1.0 to 100 mV s[1], as demonstrated in **Fig. 7B**. The symmetry of cathodic and anodic peaks suggests the reversibility of the electrochemical reactions at the HONNA. The single crystalline nature of the HONNA allows high electron mobility, facilitating the electron transfer from the Ni(OH)₂

nanobelt electroactive sites to the SS contact. Furthermore, the vertically aligned $Ni(OH)_2$ nanobelt arrays serve as extremely small electrodes. This not only enhances the surface area available for electrochemical reactions but also accelerates the ions diffusion in the electrolyte solution. As a result, it was not unexpected that the electron transfer process in the electrode and the ion diffusion in the solution were not rate-limiting processes. This was evident from the high specific capacitance and excellent rate capability demonstrated by the nanobelt arrays in the electrochemical tests, which showed a minimal decrease in capacitance even at high current densities. Typical GCD test of the HONNA electrode was performed in the potential range of 0.00.45 V (vs. Hg/Hg_2Cl_2) at a current density of 1.0 mA cm2 (**Fig. 7C**). The plateau centered at 0.27 V on GCD profile were attributed to the oxidation of $Ni(OH)_2$ to NiOOH [30]. The discharge cycle voltage shoulders at $\sim$ 0.2 V agreed well with the CV tests. The oxidation peak shifted to $\sim$ 0.27 V due to structural rearrangement. The specific capacitance of the electrode was determined using the equation, $C = \frac{I \Delta t}{S \Delta V}$ where I is the constant discharging current (mA), Δt is the discharge time (s), S is electrode surface (cm2), and ΔV is the potential range for the discharge cycle (V). The specific capacitance of the HONNA electrode was calculated to be 384 mF cm2. Once more, the low discharge time obtained from the SS substrate revealed that the capacitance derived from the substrate is negligible and it could be ignored.

The rateperformance of the HONNA was measured and evaluated in different current densities, as demonstrated in **Fig. 7D**. The capacitance retention vs. current density is demonstrated in **Fig. 7E**.

Noticeably, the nanobelt array demonstrates a high rateperformance for the supercapacitors. Moreover, the specific capacitance of 384 mF cm2 was achieved again on reversing the current density from 20 mA cm2 to 1.0 mA cm2, indicating that the HONNA structure was well-preserved even after cycling at high current densities.

To further explore the electrochemical feature of the $Ni(OH)_2$ nanobelt electrode, its cycling performance was examined by continuous cyclic voltammetry (CCV) measurements [31]–[33] over 2000 cycles at the scan rate of 250 mV s1 (**Fig. 7F**).

The specific capacitances of the HONNA were found to increase continuously through the initial 100–300 cycles, which was related to the activation process of the $Ni(OH)_2$ nanobelt electrode [34]an ultrathin 2-dimensional hierarchical nickel oxide nanobelt film array was successfully assembled and grown on a Ni substrate as a binder-free electrode material for lithium ion batteries. In the typical synthesis process, the evolution of the nickel oxide array structure was controlled by adjusting the amount of surfactant, duration of reaction time and hydrothermal temperature. By virtue of the beneficial structural characteristics of the nanobelt film array, the as-obtained NiO array electrode exhibits excellent lithium storage capacity (1035 mA h g-1 at 0.2C after 70 cycles and 839 mA h g-1 at 0.5C after 70 cycles. This activation process was highly dependent on the $Ni(OH)_2$ electrode architecture and the applied scan rate [35]–[37]. Subsequently, the specific capacitance of the nanoporous $Ni(OH)_2$ nanobelt arrays remained almost unchanged as the CV test continued. After 2000 cycles, the specific capacitance only decreased nearly 1.23% compared to initial specific capacitance, which was related to the destruction of the nanobelt structure.

After a long-term cycling stability test (the inset in **Fig. 7F**), the CV curves were still stable, which further confirmed the high cyclability and fast electrochemical reactions of the $Ni(OH)_2$ nanobelt electrode. The HONNA structure was found to exhibit a long cycling performance even at higher current densities. The CV curves obtained during successive scans revealed a high degree of synchronization, indicating the high stability of the capacitor. This stability was attributed to the
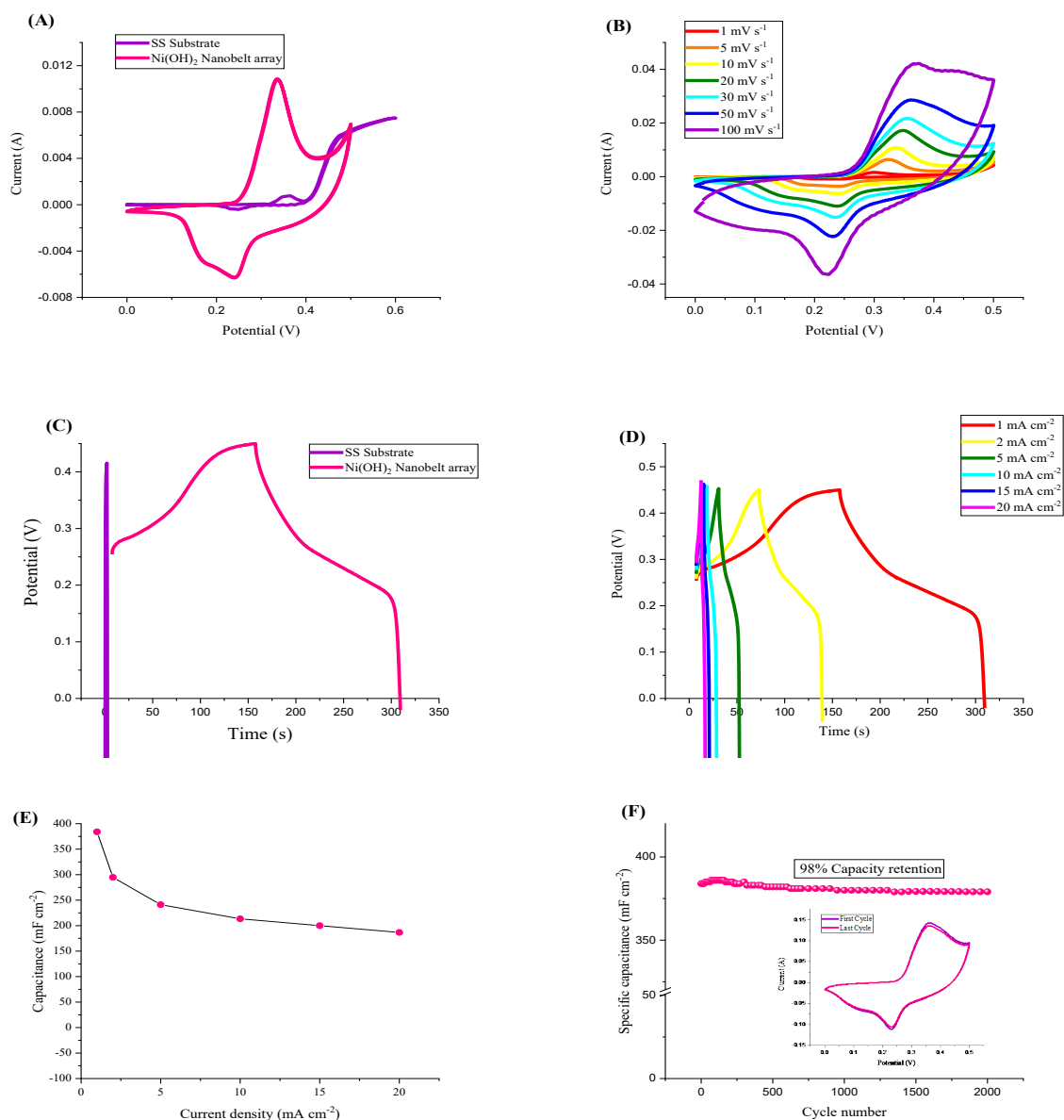
Fig. 7 CV curves of the HONNA electrode (A) at 1.0 mV s⁻¹ and (B) at different scan rates. (C) GCD curves of HONNA electrode at 1.0 mA cm², (D) GCD curve of HONNA electrode at different current densities, (E) The capacitance retention vs. current density, and (F) Capacity retention of HONNA electrode for 2000 continuous cycling at the scan rate of 250 mV s¹.

advantageous geometric features of the nanobelt structure, which facilitated ion transfer [38]. The vertical alignment of the nanobelts on the current collector was also found to assist charge transfer and contributed to stable cycling feature and high coulombic efficiency as well. **Fig. 8A** reveals the Nyquist plots of the EIS spectra obtained for the highly ordered nanoporous $Ni(OH)_2$ nanobelt ar-

ray electrode. The EIS data was fitted by an equivalent circuit (**Fig. 8B**), which comprised of the equivalent series resistance (ESR) at the electrode/electrolyte system (arising from the resistance of electrolyte solution and the electronic resistance of electrode textiles (R_s), charge transfer resistance (R_{ct}), ion diffusion resistance (Z_w), and electrochemical capacitance (Q_c) [3], [39]–[43].
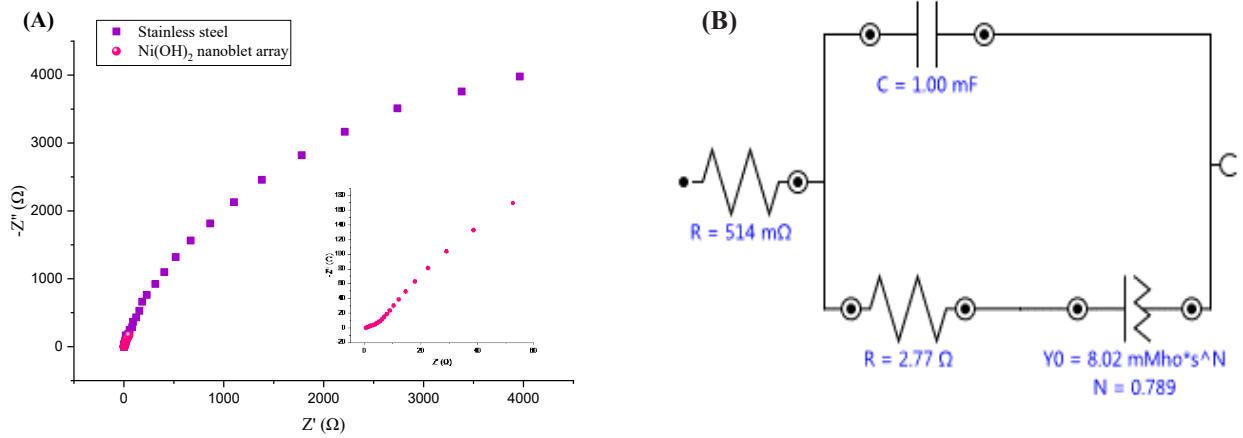
Fig. 8(A) Nyquist plot of highly ordered nanoporous Ni(OH)$_2$ nanobelt array electrode at open circuit. (Inset shows the expanded high-frequency region of the EIS spectra). **(B)** The equivalent circuit.

The EIS spectra obtained for the HONNA electrode displayed a low semicircle in the high-frequency region and a straight line in the low-frequency region. The diameter of the semicircle represents the R$_{ct}$, while the straight line reflects the diffusion of the electroactive species [44]. The Ni(OH)$_2$ nanobelt array electrodes exhibited a small semicircle, specifying low R$_{ct}$ value of the HONNA. These results suggest that HONNA are ideal for facilitating charge transfer in supercapacitor electrodes, making them suitable candidates for various electrochemical energy storage applications.

Table 1 shows the values of R$_{ct}$, R$_S$, Z$_W$, C$_{dl}$ and C$_F$ calculated from fitting of the experimental impedance spectra with equivalent circuit.

The architecture of the Ni(OH)$_2$ nanobelt array provides a large contact area between the electrode/electrolyte, facilitating rapid charge transfer and ion delivery during the charge-discharge process. Additionally, the array structure effectively mitigates the mechanical stress caused by volume expansion, resulting in improved supercapacitive properties of the electrode.

Such suitable rateperformance is associated to the HONNA deposited on the SS substrate, which form a compact structure and improve contact area between the electrode material and the substrate, and reduce the contact resistance. Due to the abundance of open voids HONNA, more electroactive species can participate in Faradaic reactions in the surrounding electrolyte. In addition, the void arrays buffer the structural change and avoid the aggregation of the active material in the ion intercalation and de-intercalation processes. Accordingly, it facilitates the ion penetration and charge transfer in the structure, which accelerates the kinetics of the electrochemical reactions during the chargedischarge cycles. Benefiting from the enhanced contact area between the electrode/electrolyte, the ion diffusion distance is shortened.

Table 1. The calculated parameters from equivalent circuit.

Element	Parameter	Value	Estimated Error (%)
R1	R	0.51352	2.025
R2	R	2.7651	9.663
C1	C	0.0010039	4.942
Q1	Y0	0.0080162	3.570
	N	0.78931	1.817
	χ^2	0.35759	

Conclusion

A facile method was developed for synthesizing highly ordered nanoporous $Ni(OH)_2$ nanobelt arrays (HONNA) using the wetchemical method. The evolution of nanobelt array architecture was adjusted by modifying the growth parameters such as temperature, time, and reactants concentrations. The NH_3 and $S_2O_8^{2-}$ concentrations played a critical role in the morphology evolution of $Ni(OH)_2$ nanobelt arrays. The nanobelt structures were utilized as the supercapacitor electrode and exhibited an improved specific capacitance of 384 mF cm² at 1.0 mA cm². In addition, the fabricated electrode demonstrated a high rateperformance, and improved specific capacitance, and cyclic stability. The unique highly ordered nanoporous nanobelt array architecture of $Ni(OH)_2$ provides more electroactive sites and minimizes electron transfer and ion diffusion path in the chargedischarge processes. As a result, this nanoporous $Ni(OH)_2$ nanobelt array electrode material is highly desirable for supercapacitors.

CRediT authorship contribution statement

Zahra Norouzi: Conceptualization, Data acquisition, Methodology, Software, Validation, Writing – original draft. **Seyed Heydar Mahmoudi Najafi:** Supervision, Validation, Writing – review & editing. **Sayed Ahmad Mozaffari:** Conceptualization, Methodology, Resources, Software, Supervision, Validation, Writing – review & editing.

Conflict of Interest

The authors declare that they have no known competing financial interests or personal relationships that could have appeared to influence the work reported in this paper.

References

[1] Amiri M., Moosavifard S. E., Davarani S. S. H., Kaverlavani S. K., and Shamsipur M., "MnCoP hollow nanocubes as novel electrode material for asymmetric supercapacitors", *Chem. Eng. J.*, 2021, 420, Part 1, 129910.

[2] Ensafi A. A., Moosavifard S. E., Rezaei B., and Kaverlavani S. K., "Engineering onion-like nanoporous $CuCo_2O_4$ hollow spheres derived from bimetal-organic frameworks for high-performance asymmetric supercapacitors", *J. Mater. Chem. A*, 2018, 6(22): 10497.

[3] Z. Norouzi, S. H. Mahmoudi Najafi, and S. A. Mozaffari, "Silver-loaded carbon sphere-in-rod 3D nano-architectures as electrode material for supercapacitors", *Diam. Relat. Mater.*, 2022, 121, 108734.

[4] Kim J.-H., Zhu K., Yan Y., Perkins C. L., and Frank A. J., "Microstructure and pseudocapacitive properties of electrodes constructed of oriented NiO-TiO$_2$ nanotube arrays", *Nano Lett.*, 2010, 10(10): 4099.

[5] Su J., Feng X., Sloppy J. D., Guo L., and Grimes C. A., "Vertically aligned WO_3 nanowire arrays grown directly on transparent conducting oxide

coated glass: synthesis and photoelectrochemical properties", *Nano Lett.*, 2011, 11(1): 203.

[6] Li J., Zhao W., Huang F., Manivannan A., and Wu N., "Single-crystalline $Ni(OH)_2$ and NiO nanoplatelet arrays as supercapacitor electrodes", *Nanoscale*, 2011, 3(12): 5103.

[7] Matsui K., Kyotani T., and Tomita A., "Hydrothermal synthesis of single-crystal $Ni(OH)_2$ nanorods in a carbon-coated anodic alumina film", *Adv. Mater.*, 2002, 14(17): 1216.

[8] Ellis B. L., Knauth P., and Djenizian T., "Three-dimensional self-supported metal oxides for advanced energy storage", *Adv. Mater.*, 2014, 26(21): 3368.

[9] Jiang J., Li Y., Liu J., Huang X., Yuan C., and Lou X. W., "Recent advances in metal oxide-based electrode architecture design for electrochemical energy storage", *Adv. Mater.*, 2012, 24(38): 5166.

[10] Xia X., Tu J., Wang X., Gu C., and Zhao X., "Hierarchically porous NiO film grown by chemical bath deposition via a colloidal crystal template as an electrochemical pseudocapacitor material", *J. Mater. Chem.*, 2011, 21(3): 671.

[11] Needham S. A., Wang G. X., and Liu H.-K., "Synthesis of NiO nanotubes for use as negative electrodes in lithium ion batteries", *J. Power Sources*, 2006, 159(1): 254.

[12] Ren W., Zhang H., Guan C., and Cheng C., "Ultrathin MoS_2 nanosheets@ metal organic framework-derived N-doped carbon nanowall arrays as sodium ion battery anode with superior cycling life and rate capability", *Adv. Funct. Mater.*, 2017, 27(32): 1702116.

[13] Wang A., Zhang M., Huang Z., Liu H., Wang Z., Song Z., *et al.*, "High-performance asymmetric supercapacitor based on Co–Mo–S/Co–Mo-LDH nanosheets grown on Co-MOF square tetrahedral structure", *J. Solid State Chem.*, 2022, 307, 122760.

[14] Narayanan R., "Single step hydrothermal synthesis of carbon nanodot decorated V_2O_5 nanobelts as hybrid conducting material for supercapacitor application", *J. Solid State Chem.*, 2017, 253, 103.

[15] Yang C.-H., Chen Y.-C., Wu C.-F., Chung R.-J., Yougbaré S., and Lin L.-Y., "Novel synthesis of ZIF67-derived $MnCo_2O_4$ nanotubes using electrospinning and hydrothermal techniques for supercapacitor", *J. Solid State Chem.*, 2022, 313, 123351.

[16] Li Y., Zhang T., Li J., Li C., Guo Z., and Ma H., "Three-dimensional nickel foam templated $MgCo_2O_4$ nanowires as an efficient catalyst for the thermal decomposition of ammonium perchlorate", *J. Solid State Chem.*, 2020, 288, 121426.

[17] Norouzi Z., Mozaffari S. A., and Mahmoudi Najafi S. H., "Three-dimensional unified electrode design using CuO embedded MnO_2 Nano-dandelions@$Ni(OH)_2$ nanoflakes as electrode material for high-performance supercapacitors", *J. Alloys Compd.*, 2023, 938, 168603.

[18] Patil U. M., Gurav K. V, Fulari V. J., Lokhande C. D., and Joo O. S., "Characterization of honeycomb-like 'β-$Ni(OH)_2$' thin films synthesized by chemical bath deposition method and their supercapacitor application", *J. Power Sources*, 2009, 188(1): 338.

[19] Gomaa M. M., RezaYazdi G., Rodner M., Greczynski G., Boshta M., and Osman M. B. S., *et al.*, "Exploring NiO nanosize structures for ammonia

sensing", *J. Mater. Sci. Mater. Electron.*, 2018, 29(14): 11870.

[20] Sarkar S., Pradhan M., Sinha A. K., Basu M., Negishi Y., and Pal T., "An aminolytic approach toward hierarchical β-Ni(OH)$_2$ nanoporous architectures: A bimodal forum for photocatalytic and surface-enhanced Raman scattering activity", *Inorg. Chem.*, 2010, 49(19): 8813.

[21] Dong L., Chu Y., and Sun W., "Controllable synthesis of nickel hydroxide and porous nickel oxide nanostructures with different morphologies", *Chem. - A Eur. J.*, 2008, 14(16): 5064.

[22] Hu J., Zhu K., Chen L., Yang H., Li Z., Suchopar A., *et al.*, "Preparation and surface activity of single-crystalline NiO (111) nanosheets with hexagonal holes: A semiconductor nanospanner", *Adv. Mater.*, 2008, 20(2): 267.

[23] Qi Y., Qi H., Lu C., Yang Y., and Zhao Y., "Photoluminescence and magnetic properties of β-Ni(OH)$_2$ nanoplates and NiO nanostructures", *J. Mater. Sci. Mater. Electron.*, 2009, 20(5): 479.

[24] Bae H. S., Shim E. H., Park J. H., and Jung H., "Γ-Ray irradiation synthesis and characterization of nickel hydroxide nanoparticles", *J. Phys. Chem. Solids*, 2012, 73(12): 1456.

[25] Yang L. X., Zhu Y. J., Tong H., Liang Z. H., Li L., and Zhang L., "Hydrothermal synthesis of nickel hydroxide nanostructures in mixed solvents of water and alcohol", *J. Solid State Chem.*, 2007, 180(7): 2095.

[26] Ni X., Zhao Q., Li B., Cheng J., and Zheng H., "Interconnected β-Ni(OH)$_2$ sheets and their morphology-retained transformation into mesostructured Ni", *Solid State Commun.*, 2006, 137(11): 585.

[27] Taşköprü T., Zor M., and Turan E., "Structural characterization of nickel oxide/hydroxide nanosheets produced by CBD technique", *Mater. Res. Bull.*, 2015, 70, 633.

[28] Boschloo G. , and Hagfeldt A., "Spectroelectrochemistry of nanostructured NiO", *J. Phys. Chem. B*, 2001, 105(15): 3039.

[29] Moosavifard S. E., Fani S., and Rahmanian M., "Hierarchical CuCo$_2$S$_4$ hollow nanoneedle arrays as novel binder-free electrodes for high-performance asymmetric supercapacitor,," *Chem. Commun.*, 2016, 52(24): 4517.

[30] Ma Z., Zhang H., Zhang Y., Zhang J., and Li Z., "Electrochemical characteristics of nanostructured NiO plates hydrothermally treated on nickel foam for Li-ion storage" *Electrochim. Acta*, 2015, 176, 1427.

[31] Naderi H. R., Sobhani-nasab A., Rahimi-Nasrabadi M., and Ganjali M. R., "Decoration of nitrogen-doped reduced graphene oxide with cobalt tungstate nanoparticles for use in high-performance supercapacitors", *Appl. Surf. Sci.*, 2017, 423, 1025.

[32] Rahimi-Nasrabadi M., Nader H. R., Karimi M. S., Ahmadi F. , and Pourmortazavi S. M., "Cobalt carbonate and cobalt oxide nanoparticles synthesis, characterization and supercapacitive evaluation", *J. Mater. Sci. Mater. Electron.*, 2016, 28, 1877.

[33] Naderi H. R., Mortaheb H. R., and Zolfaghari A., "Supercapacitive properties of nanostructured MnO$_2$/exfoliated graphite synthesized by ultrasonic vibration", *J. Electroanal. Chem.*, 2014, 719, 98.

[34] Hu N., Tang Z., and Shen P. K., "Hierarchical NiO nanobelt film array as an anode for lithium-ion batteries with enhanced electrochemical perfor-

mance", *RSC Adv.*, 2018, 8(47): 26589.

[35] Ju Z., Guo C., Qian Y., Tang B., and Xiong S., "Direct large-scale synthesis of 3D hierarchical mesoporous NiO microspheres as high-performance anode materials for lithium ion batteries", *Nanoscale*, 2014, 6(6): 3268.

[36] Wang C., Zhao Y., Su D., Ding C., Wang L., Yan D., *et al.*, "Synthesis of NiO nano octahedron aggregates as high-performance anode materials for lithium ion batteries", *Electrochim. Acta*, 2017, 231, 272.

[37] Yang W., Cheng G., Dong C., Bai Q., Chen X., Peng Z., *et al.*, "NiO nanorod array anchored Ni foam as a binder-free anode for high-rate lithium ion batteries", *J. Mater. Chem. A*, 2014, 2(47): 20022.

[38] Xu Y., Zhou M., and Lei Y., "Nanoarchitectured array electrodes for rechargeable lithium- and sodium-ion batteries", *Adv. Energy Mater.*, 2016, 6101.

[39] Asrami P. N., Mozaffari S. A., Tehrani M. S., and Azar P. A., "A novel impedimetric glucose biosensor based on immobilized glucose oxidase on a CuO-Chitosan nanobiocomposite modified FTO electrode", *Int. J. Biol. Macromol.*, 2018, 118, 649.

[40] Rahmanian R., Mozaffari S. A., Amoli H. S., and Abedi M., "Development of sensitive impedimetric urea biosensor using DC sputtered Nano-ZnO on TiO_2 thin film as a novel hierarchical nanostructure transducer", *Sens Actuators B Chem.*, 2018, 256, 760.

[41] Asrami P. N., Tehrani M. S., Aberoomand Azar P., and Mozaffari S. A., "Impedimetric glucose biosensor based on nanostructure nickel oxide transducer fabricated by reactive RF magnetron sputtering system", *J. Electroanal. Chem.*, 2017, 801, 258.

[42] S. A. Mozaffari, S. H. Mahmoudi Najafi, and Z. Norouzi, "Hierarchical NiO@Ni(OH)$_2$ nanoarrays as high-performance supercapacitor electrode material," *Electrochim. Acta*, 368, 137633, 2021.

[43] Norouzi Z., Mahmoudi Najafi S. H., and Mozaffari S. A., "Facile one-pot synthesis of binder-free $MnCo_2O_4$ nanosheets as efficient supercapacitor electrode material", *Prog. Color. Color. Coatings*, 2023, 16(3): 271.

[44] Hashemi S. A., Mousavi S. M., Naderi H. R., Bahrani S., Arjmand M., Hagfeldt, A., *et al.*, "Reinforced polypyrrole with 2D graphene flakes decorated with interconnected nickel-tungsten metal oxide complex toward superiorly stable supercapacitor", *Chem. Eng. J.*, 2021, 418, 129396.